Article

EXAFS and XANES Investigations of CuFeO Nanoparticles and CuFeO–MO (M = Sn, Ce) Nanocomposites

Venkata Krishnan, Ramakrishnan Kalai Selvan, Chanassary Ouso Augustin, Aharon Gedanken, and Helmut Bertagnolli

J. Phys. Chem. C, **2007**, 111 (45), 16724-16733 • DOI: 10.1021/jp073746t

EXAFS and XANES Investigations of $CuFe_2O_4$ Nanoparticles and $CuFe_2O_4$−MO_2 (M = Sn, Ce) Nanocomposites

Venkata Krishnan,*,†,‡ Ramakrishnan Kalai Selvan,§,|| Chanassary Ouso Augustin,§ Aharon Gedanken,|| and Helmut Bertagnolli†

Institute of Physical Chemistry, University of Stuttgart, Pfaffenwaldring 55, 70569 Stuttgart, Germany, Electropyrometallurgy Division, Central Electrochemical Research Institute, Karaikudi 630 006, India, and Department of Chemistry and Kanbar Laboratory for Nanomaterials, Bar-Ilan University Center for Advanced Materials & Nanotechnology, Bar-Ilan University, Ramat-Gan 52900, Israel

Received: May 15, 2007; In Final Form: August 1, 2007

Structural investigations were performed on combustion synthesized $CuFe_2O_4$ nanoparticles and $CuFe_2O_4$−MO_2 (M = Sn, Ce) nanocomposites in different compositions, by means of X-ray absorption fine structure spectroscopy. The studies on $CuFe_2O_4$ nanoparticles reveal that the samples have a structure analogous to that of the bulk material, wherein all the copper ions occupy the octahedral sites and the iron ions are distributed between the tetrahedral and octahedral sites. The XAFS investigations on $CuFe_2O_4$−SnO_2 and $CuFe_2O_4$−CeO_2 nanocomposites show that the incorporation of the tetravalent metal ions in the spinel lattice does not alter the local structure around copper and iron in $CuFe_2O_4$ nanoparticles. The X-ray diffraction pattern indicates $CuFe_2O_4$ as a single phase in the nanoparticles and shows the incorporation of metal ions in the spinel structure in addition to the existence of MO_2 and $CuFe_2O_4$ phases in $CuFe_2O_4$−MO_2 nanocomposites. The nanometric size of the as-synthesized materials has been confirmed by transmission electron microscopy studies. The high-resolution transmission electron microscopy investigations also confirm that $CuFe_2O_4$ exists as a single phase and reveal the composite nature of $CuFe_2O_4$−MO_2 materials.

1. Introduction

Magnetic nanomaterials have long been of scientific and technological interest. Among the magnetic materials, the spinel structured ferrites having general formula MFe_2O_4 have been used in many industrial applications. By adjusting the chemical identity of the M^{2+} cation, the magnetic configurations of MFe_2O_4 can be molecularly engineered to provide a wide range of magnetic properties.[1] Due to this versatility, MFe_2O_4 nanomaterials have been increasingly investigated for nanomagnetism and have shown great potential for many important technological applications, ranging from information storage and electronic devices to medical diagnostics and drug delivery.[2] Several studies on pure nanoferrites such as Fe_3O_4,[3] $NiFe_2O_4$,[4] $CoFe_2O_4$,[5] $ZnFe_2O_4$,[6] and $MnFe_2O_4$[7] have shown the supremacy of nanosize in view of their properties and applications.

The term nanocomposite encompasses a variety of distinctly different mixed materials at the nanometer scale. Recently, several nanocomposites encompassing ferrites have been prepared and investigated for their interesting properties. These include the magnetic−metallic nanocomposites of Fe_3O_4−Au,[8] magnetic−oxide nanocomposites of $CuFe_2O_4$−SnO_2,[9] magnetic−polymer nanocomposites of Fe_3O_4−polypyrrole,[10] and magnetic−sulfide nanocomposites of Fe_3O_4−PbS.[11] In the recent past, there has been considerable research on the structure and cation distribution in ferrite nanomaterials. Nilsen et al.[12] have studied the local structure of nanoparticulate ferrites including Fe_3O_4, $NiFe_2O_4$, $CoFe_2O_4$, and $ZnFe_2O_4$ by means of X-ray absorption fine structure (XAFS) spectroscopy and illustrated that the bulk structure extends to the nanoregime. Carta et al.[13] have investigated the formation of $CoFe_2O_4$ nanoparticles in an aerosol SiO_2 matrix using XAFS technique. The studies on cation distribution in synthetic binary, ternary, and quaternary ferrites of stoichiometry $M^{2+}M_2^{3+}O_4$, where M^{2+} = Mg, Co, Ni, Zn and M^{3+} = Fe, Al, have been elaborately performed by Henderson et al.[14] using K-edge X-ray absorption spectroscopy.

Among the ferrites, $CuFe_2O_4$ has gained significant attention in recent years.[15,16] Qi et al. reported the preparation of $CuFe_2O_4$ nanowalls using electrochemical methods,[17] and Du et al. reported the preparation of $CuFe_2O_4$ nanorods and nanodisks, using reverse micelle and hydrothermal methods.[18] In addition, $CuFe_2O_4$ nanoparticles have been prepared by co-precipitation method,[19] mechanical milling,[20] sol−gel method,[21] precipitation in polymer matrix,[22] etc., and these materials have a wide range of applications, including gas sensors,[23] CO_2 decomposition,[24] negative electrodes for Li-ion batteries,[25] hydrogen production,[26] magnetic adsorbents,[27] etc. The structural and magnetic evolution in $CuFe_2O_4$ caused by high-energy ball milling was investigated by Goya et al.,[28] wherein the researchers evidenced that the milling process reduces the average grain size of $CuFe_2O_4$ and induces cation redistribution between tetrahedral and octahedral sites.

In $CuFe_2O_4$ bulk materials, generally the copper ions occupy the octahedral sites and the iron ions occupy both the tetrahedral and octahedral sites. Among the octahedral sites, the copper ions are randomly distributed. The copper ion undergoes dsp^2 hybridization to form four square, covalent bonds in an octahedral interstice of the spinel lattice. Thus, it is bound to

* Corresponding author. Telephone: +1 215 573 7995. Fax: +1 215 573 2112. E-mail: venkrish@sas.upenn.edu.
† University of Stuttgart.
‡ Current address: Department of Chemistry, University of Pennsylvania, 231 South 34th Street, Philadelphia, PA 19104.
§ Central Electrochemical Research Institute.
|| Bar-Ilan University.

10.1021/jp073746t CCC: $37.00
Published on Web 10/11/2007

the six near-neighbor anions by four coplanar covalent bonds and two linear ionic bonds. Due to the orbital overlap, the four coplanar covalent bonds are shorter than the two ionic bonds and the elementary octahedron becomes distorted from cubic to tetragonal symmetry.[29] Bulk $CuFe_2O_4$ is tetragonal below 760 °C and the axial ratio c/a decreases monotonically from room temperature to 700 °C. Above 760 °C, the copper ions are distributed in the anion interstices and the lattice is cubic.[30] It is reported that, at room temperature, 88% of copper ions are in octahedral sites and, at 700 °C, the concentration of copper ions decrease to 74%. The fact that copper ions migrate from octahedral to tetrahedral sites indicates that they can be readily accommodated in tetrahedral sites although, because of square-bond formation, it is more stable in octahedral sites.[30] In ferrites, the divalent and trivalent metal ions occupy the site for which they have higher crystal field stability energy (CFSE).[31,32] For example, the Fe^{2+} cation has higher octahedral CFSE and occupies the octahedral sites, but Fe^{3+} cations have zero CFSE and, therefore, can occupy either tetrahedral or octahedral sites depending on the preference energy of the second cation in the structure.[33] In bulk $CuFe_2O_4$, the iron ions are arbitrarily distributed between the tetrahedral and octahedral sites. The distribution and valence of the metal ions on the octahedral and tetrahedral sites determines the materials' magnetic and electronic properties. Hence, it is noteworthy to study whether the $CuFe_2O_4$ nanoparticles have a structure similar to that of bulk $CuFe_2O_4$ and to also investigate the cation distribution in the nanoparticles.

This work is a part of a comprehensive study concerning the structure and properties of $CuFe_2O_4$ based nanocomposites. We have previously reported the dielectric,[9] magnetic,[34] and electrochemical[35] properties of $CuFe_2O_4-SnO_2$ nanocomposites. Since the functional properties of these materials are strongly dependent on the structure, it is important to investigate it in detail. In this paper, we report the investigations on the local structure and cation distribution in $CuFe_2O_4$ nanoparticles and the influence of SnO_2 and CeO_2 on the structure and coordination geometry of $CuFe_2O_4$ based nanocomposites.

Elemental selectivity is one of the main characteristics of X-ray absorption fine structure (XAFS) spectroscopy, which makes it suitable to analyze problems of this nature. XAFS spectroscopy using a synchrotron radiation source is a powerful tool to determine the local structure of a specific atom, regardless of the physical state of the sample. The extended X-ray absorption fine structure (EXAFS) spectroscopy provides information about the coordination number, the nature of the scattering atoms surrounding the absorbing atom, the interatomic distance between absorbing and backscattering atoms, and the Debye−Waller factor, which accounts for the disorders due to the static displacements and thermal vibrations.[36,37] The X-ray absorption near-edge structure (XANES) region provides information about oxidation states, vacant orbitals, electronic configuration, and site symmetry of the absorbing atom.[38] The XANES spectra may have preedge peaks related to the electronic transitions taking place between the different shells. The strength of such preedge peaks strongly depends on the coordination geometry around the absorbing atom and can therefore be used as an indicator of geometrical changes.[39,40]

2. Experimental Section

2.1. Sample Preparation. The nanocrystalline $CuFe_2O_4$ and $CuFe_2O_4-xMO_2$ (x = 5%, 20%—percentage by weight; M = Sn, Ce) nanocomposites were prepared by urea−nitrate combustion method. The synthesis procedure and the thermodynamical calculations of parent $CuFe_2O_4$ were reported earlier.[41] In the preparation of $CuFe_2O_4-SnO_2$ nanocomposites, the stoichiometric quantities of $Cu(NO_3)_2\cdot 6H_2O$, $Fe(NO_3)_3\cdot 9H_2O$, $SnCl_4$, HNO_3, and $CO(NH_2)_2$ were dissolved in 100 mL of distilled water, and in the preparation of $CuFe_2O_4-CeO_2$ nanocomposites, the stoichiometric quantities of $Cu(NO_3)_2\cdot 6H_2O$, $Fe(NO_3)_3\cdot 9H_2O$, $Ce(NO_3)_3$, and $CO(NH_2)_2$ were dissolved in 100 mL of distilled water. For both nanocomposites, the mixed nitrate−urea solution was heated at 110 °C, with continuous stirring. After the evaporation of an excess of water, a highly viscous gel was obtained. Subsequently, the gel was ignited at 300 °C to evolve the undesirable gaseous products, resulting in the formation of desired product in the form of foamy powder. Finally, the powder was sintered at 1100 °C for 5 h to obtain ultrafine powders of $CuFe_2O_4-MO_2$ nanocomposites.

2.2. Measurements. The transmission mode XAFS measurements were performed on the nanocomposite ferrite samples at Cu K-edge at 8979 eV, Fe K-edge at 7112 eV, and Ce L_{III}-edge at 5723 eV at the beamline A1, at Hamburger Synchrotron Radiation Laboratory (HASYLAB), Hamburg, Germany. The samples were measured with a Si(111) double crystal monochromator at ambient conditions, and ion chambers filled with nitrogen were used to measure the incident and transmitted intensities. The positron energy was 4.45 GeV, and the beam current was between 90 and 130 mA during the measurements. The samples in solid state were embedded in cellulose matrix and pressed into a pellet. The concentration was adjusted to yield an extinction of 1.5. The prepared pellets were encapsulated by Kapton tape and mounted on to sample holders for XAFS measurements. The compound formation, phase purity, and crystallinity of the ferrite materials were identified by X-ray powder diffraction (XRD) pattern measured using a X-ray diffractometer (Rigaku Dmax/2C, Japan with Cu Kα radiation; λ = 1.5405 Å). The particle size was analyzed through transmission electron microscopy (TEM) using a JEOL-JEM 100SX microscope operating at an accelerating voltage of 200 kV in high-resolution (HR) mode. The TEM specimen was prepared by dissolving a small quantity of the sample in ethanol and sonicating the solution for 10 min in a vial placed in a sonication bath. A few drops of the sample suspension were deposited on a copper grid (400 mesh, Spi suppliers, West Chester, PA) coated with carbon film, and they were allowed to dry in air, at ambient conditions.

2.3. EXAFS Evaluation. In the data analysis, the program WINXAS[42] was used for normalization and the program AUTOBK[43] was used for the removal of background. The employed method subtracts a spline that best eliminates the nonstructural portion from the measured spectrum. The spline used to approximate the background is a third-order polynomial spline with knots that are equally spaced in k-space, where one degree of freedom in the spline is allowed. Data evaluation in k-space was performed according to the curved wave formalism of the program EXCURV98[44] with XALPHA phase and amplitude functions. The mean free paths of the scattered electrons were calculated from the imaginary part of the potential (VPI set to −4.00), the amplitude factor AFAC was fixed at 0.8, and a Fermi energy shift E_F was introduced to give a best fit to the data. The structural parameters were obtained by nonlinear least-squares fitting in k-space with k^3 weighting and with k-ranges chosen to be as large as possible. In the fitting procedure, the various parameters, i.e., coordination number, interatomic distance, Debye−Waller factor, and Fermi energy value, were determined by iterations. For clarity reasons, the EXAFS spectrum and the Fourier transform plot are shifted

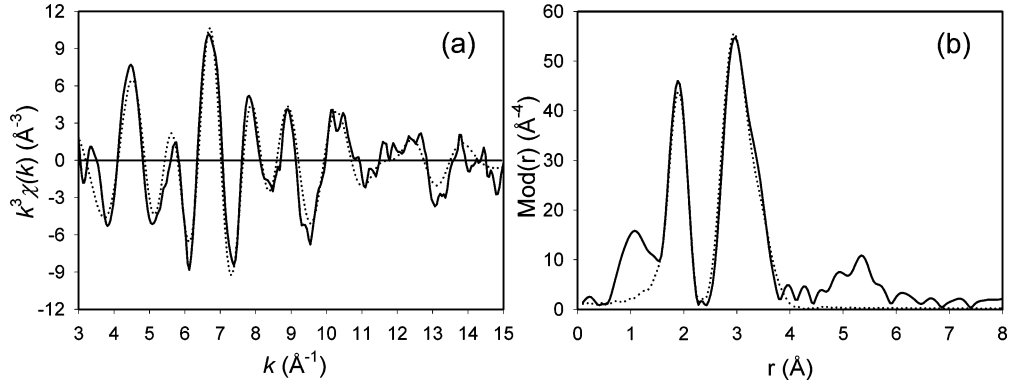

Figure 1. Experimental (—) and calculated (···) EXAFS functions (a) and their Fourier transforms (b) for $CuFe_2O_4$ nanoparticles measured at the Cu K-edge.

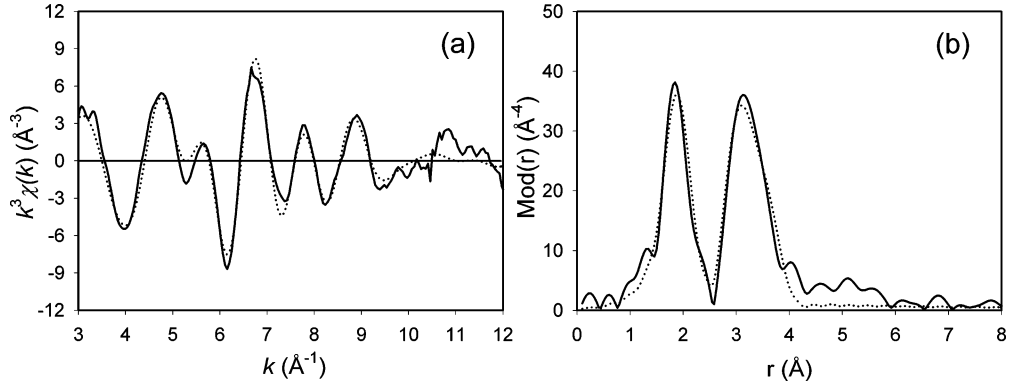

Figure 2. Experimental (—) and calculated (···) EXAFS functions (a) and their Fourier transforms (b) for $CuFe_2O_4$ nanoparticles measured at the Fe K-edge.

along the ordinate axis in many figures. The exact zero position of the EXAFS spectrum and that of the corresponding Fourier transform can be obtained by observing the value on the ordinate axis at the intersection point.

2.4. XANES Evaluation. The XANES spectra directly reflect the changes in the structural and electronic properties as the method involves the excitation of a photoelectron into low-lying empty states of the central atom. For a given environment, the main peak is broadened by disorders in the nearest neighbor distances and secondary peaks occurring a few tens of electronvolts above the main peak correspond to multiple scattering from neighboring atom shells.[45] The lower conduction bands of transition metal oxides are primarily composed of metal 3d orbitals, while the upper valence bands are mainly composed of oxygen 2p orbitals.[46] Due to the crystal field of the lattice, the 3d orbitals of the lower conduction bands are split into subbands that gained p-character by mixing with p-orbitals of the central metal atom or neighboring oxygen atoms.[47] The preedge features in XANES spectra of transition metal K-edge could be attributed to (a) 1s → 3d quadrupole transitions,[48] (b) dipole-allowed transitions due to 3d−4p mixing of the metal, and (c) d−p mixing between the metal atom and ligands through bonding and multiple scattering involving the same atoms with different scattering paths.[49] Therefore, the positions of the preedge peaks directly reflect the crystal field splitting of 3d orbital subbands, and intensities of the preedge features are sensitive to the local coordination geometry of the metal atom. In the case of inner transition elements, there is a large mixing of metal 4f and oxygen 2p orbitals. In the L_{III}-edge XANES region of the f-block elements, the main peak due to 2p → 5d electronic transition is influenced by many-body effects.[50] In general, an increase in the oxidation state of the metal atom causes a shift to higher energies and a decrease in the degree of centrosymmetry of the metal atom environment leads to an increase in the preedge peak intensity.

3. Results and Discussion

3.1. $CuFe_2O_4$ Nanoparticles. The experimentally determined and the theoretically calculated EXAFS functions in *k*-space and their Fourier transforms in real space for $CuFe_2O_4$ nanoparticles, measured at the Cu and Fe K-edges, are shown in Figures 1 and 2, respectively. The corresponding structural parameters are tabulated in Table 1. In the evaluation of the EXAFS function, it should be considered that depending on the site occupancy by the cation, the cation−oxygen and the cation−cation distances differ very much. For the analysis at the Cu K-edge, a four-shell model is fitted. The analysis indicates two distinct oxygen shells at 1.97 and 2.21 Å distance with four and two backscatterers, respectively. This result clearly reveals that the copper ions occupy the octahedral interstices in the spinel lattice, wherein each copper atom forms four short coplanar covalent bonds and two long linear ionic bonds with the six near-neighboring oxygen atoms. The third shell was determined at 2.94 Å distance with about six metal backscatterers. This distance is typical of the cations occupying the octahedral sites (B sites), when the absorber is in an octahedral site[51] and is mentioned as M_B in the tables. In the case of $CuFe_2O_4$, both copper and iron atoms occupy the B sites and it was not possible to discriminate their individual contributions by means of EXAFS spectroscopy; therefore they were fitted together as a single metal shell with iron amplitude and phase functions. The fourth shell was found at 3.40 Å, a distance typical for the cations occupying the tetrahedral sites (A sites),[51] and is cited as M_A in the tables. This shell could be fitted with about three metal backscatterers using iron amplitude and phase

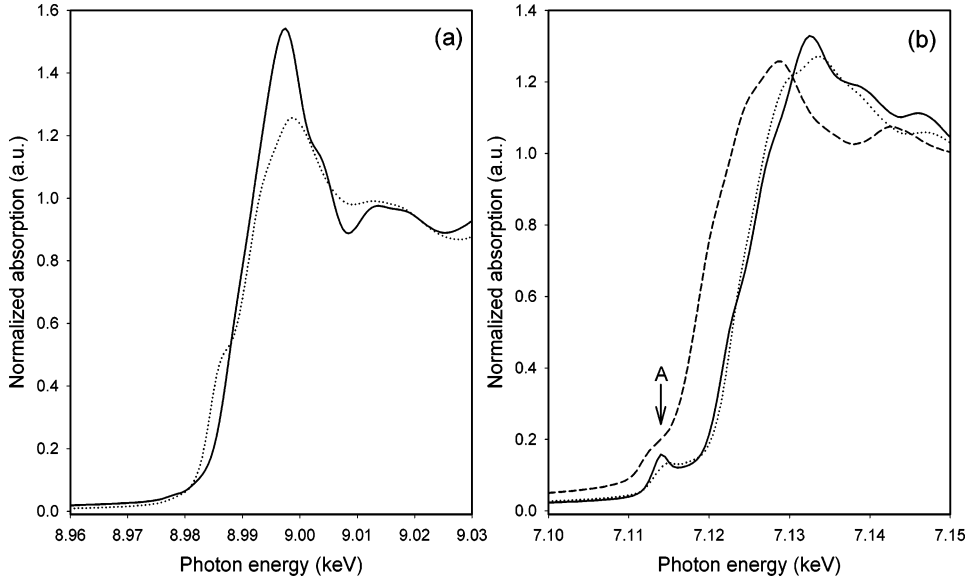

Figure 3. XANES region (a) of $CuFe_2O_4$ (—) along with the reference CuO (•••) measured at the Cu K-edge. XANES region and (b) of $CuFe_2O_4$ (—) along with the references Fe_2O_3 (•••) and FeO (--) measured at the Fe K-edge.

TABLE 1: EXAFS Obtained Structural Parameters for $CuFe_2O_4$ Nanoparticles

sample	A−Bs[a]	N [b]	r [c] (Å)	σ [d] (Å)	E_F [e] (eV)	k-range (Å^{-1})	R-factor
$CuFe_2O_4$	Cu−O	3.7 ± 0.4	1.97 ± 0.02	0.067 ± 0.007	7.111	2.97−15.04	39.31
	Cu−O	1.7 ± 0.2	2.21 ± 0.02	0.095 ± 0.010			
	Cu−M_B[f]	6.4 ± 1.0	2.94 ± 0.03	0.102 ± 0.015			
	Cu−M_A[g]	3.1 ± 0.6	3.40 ± 0.04	0.110 ± 0.022			
	Fe−O	5.1 ± 0.5	1.95 ± 0.02	0.107 ± 0.011	4.850	2.97−12.03	28.39
	Fe−M_B	5.7 ± 0.9	2.99 ± 0.03	0.122 ± 0.018			
	Fe−$M_{A/B}$[h]	5.6 ± 1.1	3.45 ± 0.04	0.122 ± 0.024			

[a] A, absorber; Bs, backscatterers. [b] N, coordination number. [c] r, interatomic distance. [d] σ, Debye−Waller factor, with its calculated deviation. [e] E_F, Fermi energy. [f] M_B, metal backscatterers occupying the octahedral sites. [g] M_A, metal backscatterers occupying the tetrahedral sites. [h] $M_{A/B}$, metal backscatterers occupying both tetrahedral and octahedral sites.

TABLE 2: Edge Energy and Oxidation States for the Different Ferrite Nanocomposites along with the Reference Compounds

sample	element	oxidation state	absorption edge (eV)
$CuFe_2O_4$	Cu	+2	8991.0
	Fe	+3	7124.0
$CuFe_2O_4$−5% SnO_2	Cu	+2	8991.0
	Fe	+3	7124.0
$CuFe_2O_4$−20% SnO_2	Cu	+2	8991.0
	Fe	+3	7124.5
$CuFe_2O_4$−5% CeO_2	Cu	+2	8991.0
	Fe	+3	7124.0
	Ce	+4	5717.0
$CuFe_2O_4$−20% CeO_2	Cu	+2	8991.0
	Fe	+3	7124.0
	Ce	+4	5717.0
CuO	Cu	+2	8991.5
Fe_2O_3	Fe	+3	7124.0
FeO	Fe	+2	7119.5
CeO_2	Ce	+4	5716.5

functions. The obtained structural parameters are in agreement with the values reported for bulk $CuFe_2O_4$ in the space group $I4_1/amd$.[52] The results reveal that all the copper atoms occupy the octahedral sites and their occupancy of tetrahedral sites could not be validated.

For the analysis at the Fe K-edge, a three shell model is employed. The first shell is centered at 1.95 Å distance and could be fitted with about five oxygen backscatterers. The asymmetric shape of this first peak in the Fourier transform plot corresponds with the two different Fe−O bond distances attributable to the presence of iron atoms on the tetrahedral and octahedral sites. Similar observation has also been reported for NiZn−ferrite films.[53] In the Fourier transform plot, the second peak is broad and spreads over a wide range, indicating the presence of both the second and the third shells in it. This is also an indication that iron atoms occupy both tetrahedral and octahedral sites. The second shell could be fitted at a distance of 2.99 Å with about six metal backscatterers occupying the B sites, as this distance is typical of a cation present at the octahedral sites. The third shell found at 3.45 Å distance could be fitted with about six metal backscatterers. This distance is typical for metal backscatterers occupying tetrahedral sites, when the absorber is in an octahedral site. However, this distance is also characteristic for metal backscatterers occupying octahedral sites, when the absorber is in a tetrahedral site. Since the results illustrate the presence of iron in both tetrahedral and octahedral sites, the contributions for the third shell comes from the cations occupying both A and B sites, and is mentioned as $M_{A/B}$ in the tables. In the evaluation of the second and third shells, iron amplitude and phase functions were used. For all three shells, the determined Debye−Waller factor values were higher than normal, indicating high disorder in the distribution of iron atoms between the tetrahedral and octahedral sites. The first shell Fe−O bond distance of 1.95 Å determined from EXAFS analysis is an average of the tetrahedrally and octahedrally coordinated iron atoms. In bulk $CuFe_2O_4$ in the space group $I4_1/amd$, the Fe−O distance is 1.74 Å for the iron atoms on the A sites and 2.14 Å for the iron atoms on the B sites.[52] Using these values, the percentage distribution of iron atoms between the tetrahedral and octahedral interstices can be estimated employing the procedure reported in the literature.[54] The calculations indicate that 58% of iron ions are in A sites and

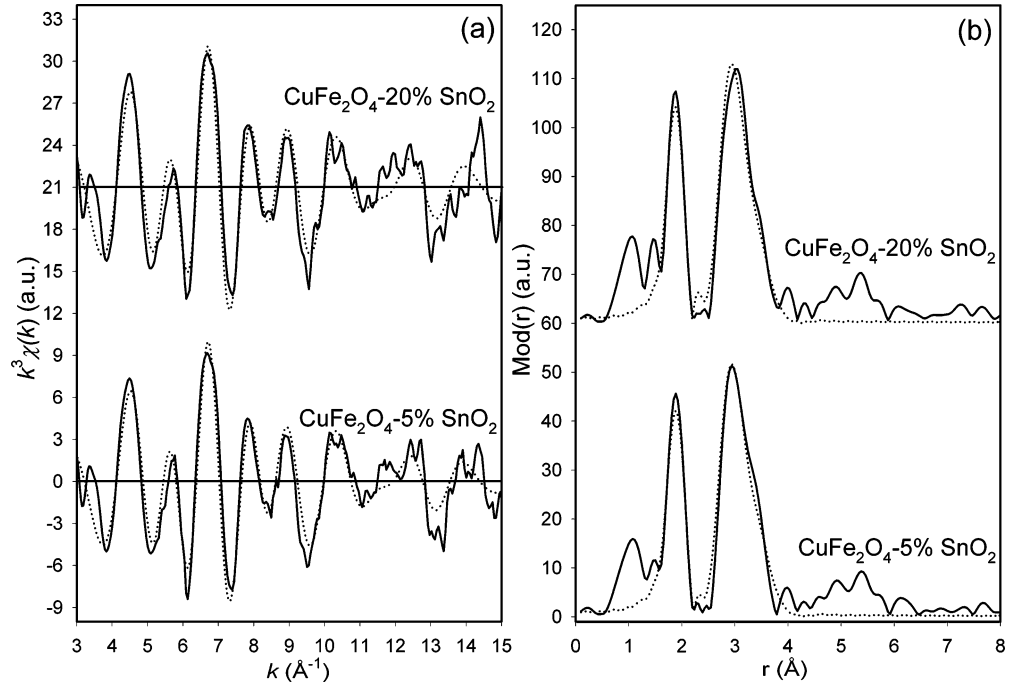

Figure 4. Experimental (—) and calculated (···) EXAFS functions (a) and their Fourier transforms (b) for $CuFe_2O_4-SnO_2$ samples measured at Cu K-edge.

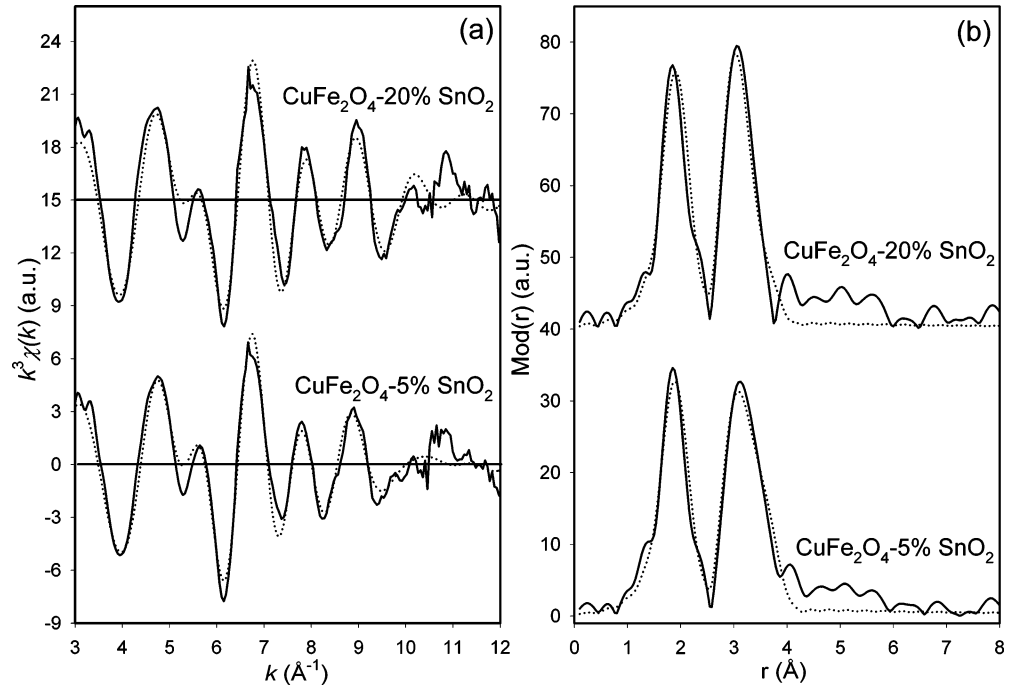

Figure 5. Experimental (—) and calculated (···) EXAFS functions (a) and their Fourier transforms (b) for $CuFe_2O_4-SnO_2$ samples measured at Fe K-edge.

42% are in B sites. Furthermore, the average coordination number calculated on the basis of the same literature[54] results in a value of 4.8, which is in agreement with the value of 5.1 determined from EXAFS analysis. In addition, it is noteworthy to mention that Sahastabudhe and Vaingankar[55] have illustrated the covalent bonding nature of copper ferrite by means of EXAFS spectroscopy considering the octahedral/tetrahedral cation−oxygen bonding and the electronegativity difference between cation and oxygen ion. Yang et al.[56] have successfully employed EXAFS to study the copper cation inversion in $CuFe_2O_4$ as a function of saturation magnetization.

The XANES investigations were performed to complement the results obtained from EXAFS studies. The edge energy and oxidation states determined from the XANES analysis for $CuFe_2O_4$ nanoparticles at the Cu and Fe K-edges are tabulated in Table 2. The XANES region of $CuFe_2O_4$ nanoparticles measured at the Cu K-edge is shown along with the reference CuO in Figure 3.

In bulk $CuFe_2O_4$, the X-ray diffraction measurements at room temperature reported by Ohnishi and Teranishi[57] indicate that approximately 10% of the copper atoms occupy the tetrahedral sites, and theory[58] suggests that the tetrahedrally coordinated copper ions should have +1 valence. It follows that, for such a sample, in the XANES region, one would expect to observe the contributions from a mixture of 90% Cu^{2+} and 10% Cu^{1+} cations. In such a case there would be a small preedge peak

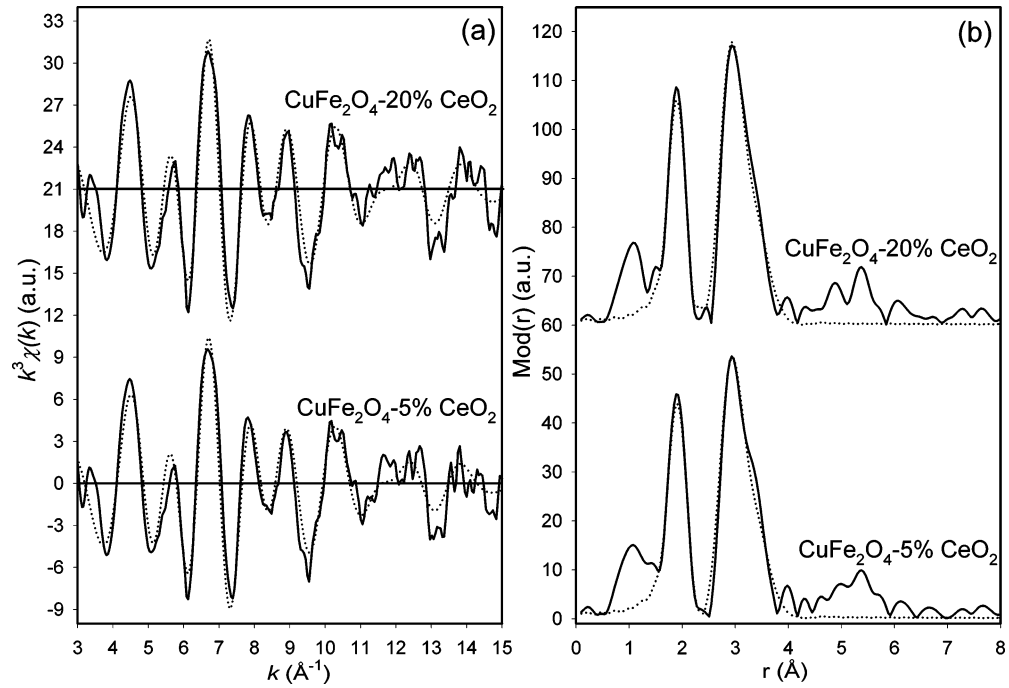

Figure 6. Experimental (—) and calculated (···) EXAFS functions (a) and their Fourier transforms (b) for $CuFe_2O_4-CeO_2$ nanocomposites measured at the Cu K-edge.

TABLE 3: EXAFS Obtained Structural Parameters for $CuFe_2O_4-SnO_2$ Nanocomposites

sample	A−Bs[a]	N [b]	r [c] (Å)	σ [d] (Å)	E_F [e] (eV)	k-range (Å^{-1})	R-factor
$CuFe_2O_4-5\%\ SnO_2$	Cu−O	3.5 ± 0.4	1.96 ± 0.02	0.067 ± 0.007	7.668	2.96−15.04	39.59
	Cu−O	1.5 ± 0.2	2.18 ± 0.02	0.077 ± 0.008			
	Cu−M_B[f]	6.3 ± 1.0	2.93 ± 0.03	0.105 ± 0.016			
	Cu−M_A[g]	3.2 ± 0.6	3.40 ± 0.04	0.114 ± 0.023			
	Fe−O	5.1 ± 0.5	1.96 ± 0.02	0.112 ± 0.011	4.678	2.99−12.02	27.72
	Fe−M_B[f]	5.3 ± 0.8	2.99 ± 0.03	0.122 ± 0.018			
	Fe−$M_{A/B}$[h]	4.6 ± 0.9	3.45 ± 0.04	0.122 ± 0.024			
$CuFe_2O_4-20\%\ SnO_2$	Cu−O	3.6 ± 0.4	1.96 ± 0.02	0.063 ± 0.006	7.957	2.95−15.04	43.64
	Cu−O	1.8 ± 0.2	2.17 ± 0.02	0.077 ± 0.008			
	Cu−M_B[f]	6.6 ± 1.0	2.93 ± 0.03	0.105 ± 0.016			
	Cu−M_A[g]	3.2 ± 0.6	3.39 ± 0.04	0.114 ± 0.023			
	Fe−O	5.2 ± 0.5	1.97 ± 0.02	0.107 ± 0.011	4.887	2.97−12.03	32.47
	Fe−M_B[f]	6.5 ± 1.0	2.99 ± 0.03	0.118 ± 0.018			
	Fe−$M_{A/B}$[h]	4.7 ± 0.9	3.39 ± 0.04	0.145 ± 0.029			

[a] A, absorber; Bs,backscatterers. [b] N, coordination number. [c] r, interatomic distance. [d] σ, Debye−Waller factor, with its calculated deviation. [e] E_F, Fermi energy. [f] M_B, metal backscatterers occupying the octahedral sites. [g] M_A, metal backscatterers occupying the tetrahedral sites. [h] $M_{A/B}$, metal backscatterers occupying both tetrahedral and octahedral sites.

signifying the contributions from Cu^{1+} cations.[59,60] However, in the $CuFe_2O_4$ nanoparticles the above-mentioned preedge peak could not be evidenced, indicating the absence of Cu^{1+} cations. This in turn reveals that there are no tetrahedrally coordinated copper ions, which is in agreement with the EXAFS studies. In addition, the similarity in the values for the absorption edge of $CuFe_2O_4$ nanoparticles and CuO reveals that copper is in the the +2 oxidation state in the nanoparticles.

The XANES region of $CuFe_2O_4$ nanoparticles measured at the Fe K-edge is shown along with the references Fe_2O_3 and FeO in Figure 3. The comparison of the absorption edge values of $CuFe_2O_4$ nanoparticles with those of Fe_2O_3 and FeO indicates that iron is in the +3 oxidation state in the nanoparticles. The XANES region of $CuFe_2O_4$ nanoparticles show an intense preedge peak (marked as A), which is characteristic of Fe^{3+} cations in tetrahedral sites. This preedge peak is attributed to 1s → 3d electronic transition. Since 1s and 3d states are centrosymmetric, the transition probability should be small. When the ion is in a centrosymmetric octahedral site, quadrupole interactions are allowed. But when the ion is in a noncentrosymmetric tetrahedral site, dipole interactions are allowed, wherein the mixing of 4p and 3d orbitals intensifies the absorption.[61] In $CuFe_2O_4$ nanoparticles, the preedge peak is more pronounced due to the noncentrosymmetric tetrahedral crystal field. The XANES studies suggest that iron ions occupy more of A sites than B sites, which is in agreement with the EXAFS studies.

3.2. $CuFe_2O_4-SnO_2$ Nanocomposites. The experimentally determined and the theoretically calculated EXAFS functions in k-space and their Fourier transforms in real space for the nanocomposites of $CuFe_2O_4$ containing 5 and 20% (percentage by weight) SnO_2, measured at the Cu K-edge, are shown in Figure 4 and those measured at the Fe K-edge are shown in Figure 5. The fitted parameters are given in Table 3. The EXAFS determined parameters for the $CuFe_2O_4-SnO_2$ (both 5 and 20%) nanocomposites at Cu and Fe K-edges resembled the structural parameters of their corresponding counterparts without SnO_2, indicating that the incorporation of tin ions into the $CuFe_2O_4$ lattice does not lead to significant local structural changes around Cu and Fe ions in $CuFe_2O_4$ nanoparticles. The XRD investigations reported earlier[9] revealed changes in the

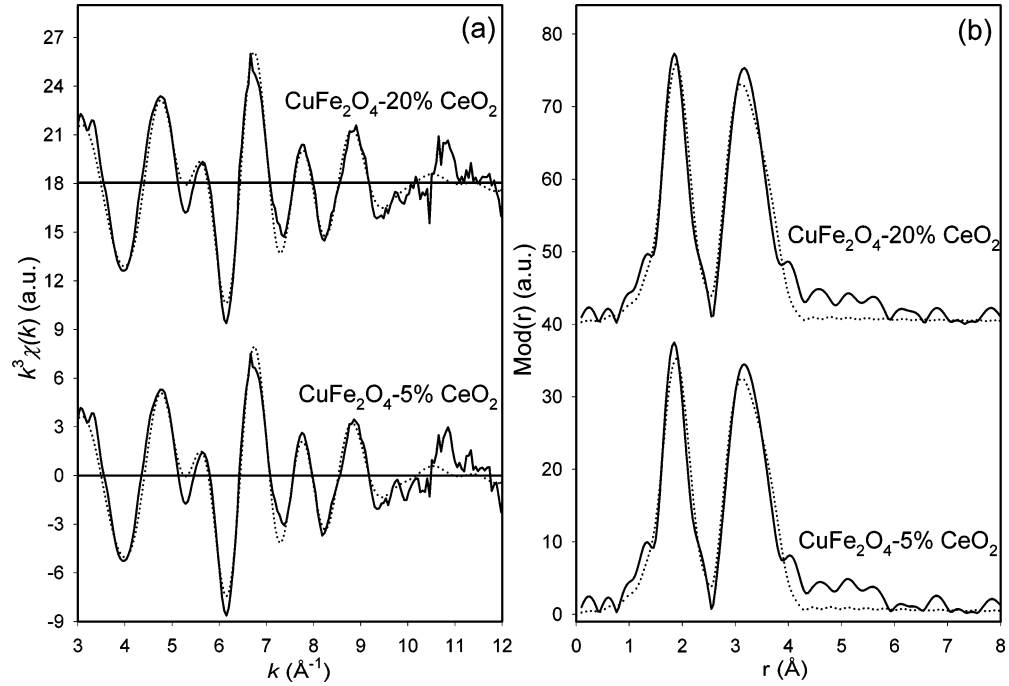

Figure 7. Experimental (—) and calculated (···) EXAFS functions (a) and their Fourier transforms (b) for $CuFe_2O_4-CeO_2$ nanocomposites measured at the Fe K-edge.

TABLE 4: EXAFS Obtained Structural Parameters for $CuFe_2O_4-CeO_2$ Nanocomposites

sample	A−Bs[a]	N[b]	r [c] (Å)	σ [d] (Å)	E_F [e] (eV)	k-range (Å^{-1})	R-factor
$CuFe_2O_4-5\%$ CeO_2	Cu−O	3.7 ± 0.4	1.97 ± 0.02	0.067 ± 0.007	7.144	2.97−15.04	41.33
	Cu−O	1.6 ± 0.2	2.22 ± 0.02	0.095 ± 0.010			
	Cu−M_B[f]	6.3 ± 1.0	2.94 ± 0.03	0.102 ± 0.015			
	Cu−M_A[g]	3.0 ± 0.6	3.40 ± 0.04	0.112 ± 0.022			
	Fe−O	5.1 ± 0.5	1.95 ± 0.02	0.110 ± 0.011	4.802	2.96−12.03	28.06
	Fe−M_B[f]	5.3 ± 0.8	2.99 ± 0.03	0.122 ± 0.018			
	Fe−$M_{A/B}$[h]	6.0 ± 1.2	3.45 ± 0.04	0.122 ± 0.024			
$CuFe_2O_4-20\%$ CeO_2	Cu−O	3.6 ± 0.4	1.97 ± 0.02	0.063 ± 0.006	7.516	2.96−15.04	40.02
	Cu−O	1.7 ± 0.2	2.20 ± 0.02	0.084 ± 0.008			
	Cu−M_B[f]	6.3 ± 1.0	2.93 ± 0.03	0.100 ± 0.015			
	Cu−M_A[g]	3.2 ± 0.6	3.40 ± 0.04	0.112 ± 0.022			
	Fe−O	5.1 ± 0.5	1.95 ± 0.02	0.107 ± 0.011	4.750	2.99−12.02	27.25
	Fe−M_B[f]	5.4 ± 0.8	2.99 ± 0.03	0.122 ± 0.018			
	Fe−$M_{A/B}$[h]	5.8 ± 1.2	3.45 ± 0.04	0.122 ± 0.024			

[a] A, absorber; Bs, backscatterers. [b] N, coordination number. [c] r, interatomic distance. [d] σ, Debye−Waller factor, with its calculated deviation. [e] E_F, Fermi energy. [f] M_B, metal backscatterers occupying the octahedral sites. [g] M_A, metal backscatterers occupying the tetrahedral sites. [h] $M_{A/B}$, metal backscatterers occupying both tetrahedral and octahedral sites.

TABLE 5: XRD Obtained Lattice Parameters for $CuFe_2O_4$ and $CuFe_2O_4-CeO_2$ Nanocomposites

sample	a (Å)	c (Å)
$CuFe_2O_4$	8.2740 ± 0.0003	8.4814 ± 0.0002
$CuFe_2O_4-5\%$ CeO_2	8.2581 ± 0.0002	8.6881 ± 0.0001
$CuFe_2O_4-20\%$ CeO_2	8.2607 ± 0.0002	8.6521 ± 0.0003

lattice parameter values of $CuFe_2O_4$ due to the addition of SnO_2, which could be taken as evidence of incorporation of tin ions into the spinel lattice. Furthermore, the XRD pattern revealed the presence of Bragg peaks representative of SnO_2 and $CuFe_2O_4$ phases, indicating that the incorporation is minimal and the excess of SnO_2 phase segregates. Because the SnO_2 content was very low in the samples, unambiguous quantification of the different phases was not possible. The TEM investigations on the as-synthesized samples indicate that the $CuFe_2O_4-SnO_2$ samples are composed on 20−30 nm sized particles.[9] In addition, the HRTEM studies also showed the phase segregation of SnO_2 and $CuFe_2O_4$ nanoparticles.[9] The Cu−Sn or Fe−Sn distances could not be determined from EXAFS analysis as the

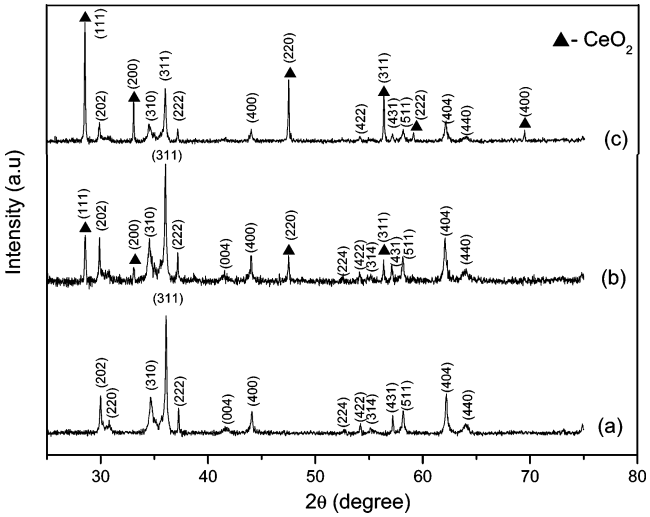

Figure 8. XRD patterns of $CuFe_2O_4$ (a), $CuFe_2O_4-5\%$ CeO_2 (b), and $CuFe_2O_4-20\%$ CeO_2 (c).

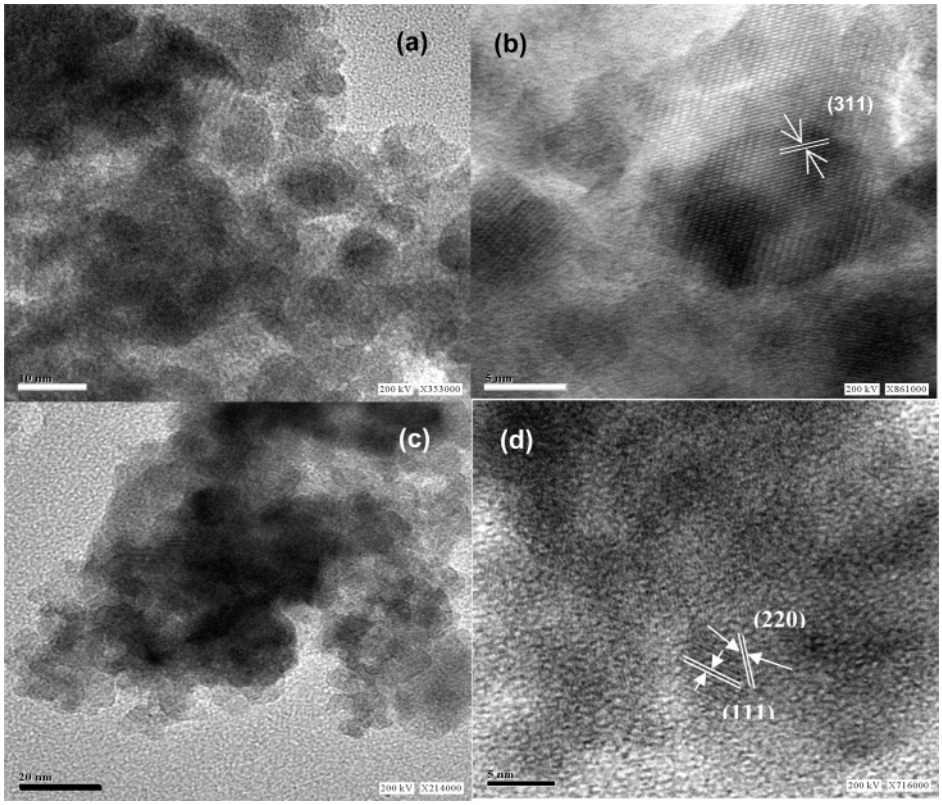

Figure 9. TEM (a) and HRTEM (b) images of $CuFe_2O_4$ nanoparticles. TEM (c) and HRTEM (d) images of $CuFe_2O_4-5\%$ CeO_2 nanocomposites. The scale bar in (a) is 10, (b) is 5, (c) is 20, and (d) is 5 nm.

contributions from the tin atoms are lower than the contributions from the core $CuFe_2O_4$ nanoparticles.

The XANES region of $CuFe_2O_4-SnO_2$ nanocomposites at the Cu and Fe K-edge are similar to those in $CuFe_2O_4$ nanoparticles. The edge energy and oxidation states determined from the XANES analysis at the Cu and Fe K-edges are listed in Table 2. The comparison of the absorption edge values of $CuFe_2O_4-SnO_2$ nanocomposites with the corresponding reference compounds indicate that copper is in the +2 and iron is in the +3 oxidation state in these nanocomposites.

3.3. $CuFe_2O_4-CeO_2$ Nanocomposites. The experimentally determined and the theoretically calculated EXAFS functions in *k*-space and their Fourier transforms in real space for the nanocomposites of $CuFe_2O_4$ containing 5 and 20% (percentage by weight) CeO_2, measured at the Cu K-edge, are shown in Figure 6 and those measured at the Fe K-edge are shown in Figure 7. The determined structural parameters are tabulated in Table 4. In this case as well, the structural parameters obtained from both Cu and Fe K-edge analyses are similar to those of $CuFe_2O_4$ nanoparticles. There are also no variations in the parameters obtained for the 5 and 20% CeO_2 containing samples, revealing that the addition of CeO_2 does not alter the local structure around Cu and Fe ions in $CuFe_2O_4$ nanoparticles. In this case as well, the distances corresponding to Cu−Ce and Fe−Ce could not be determined from EXAFS analysis due to the same reasons mentioned earlier for $CuFe_2O_4-SnO_2$ nanocomposites. Due to the low absorption jump at the Ce L_{III}-edge because of high extinction and low CeO_2 content in the samples, the signal-to-noise ratio was poor in the measured spectrum and, hence, the EXAFS data could not be evaluated. Due to the inability to perform detailed EXAFS analysis at the Ce L_{III}-edge, the possibility of the Cu−O−Ce and Fe−O−Ce interactions could not be unequivocally addressed.

The XRD patterns for 1100 °C sintered 5 and 20% (percentage by weight) CeO_2 containing $CuFe_2O_4$ nanocomposites are shown in Figure 8, along with the pattern of $CuFe_2O_4$ nanoparticles. The obtained lattice parameters are tabulated in Table 5. It can be observed that the XRD patterns are characterized by well-defined sharp and high-intensity peaks with definite *d* and *h k l* values. The mean crystallite size was calculated from the width of the most intense diffraction peak using the Scherrer equation[62] and the crystallite dimensions were found to be 15, 41, and 31 nm for $CuFe_2O_4$ nanoparticles, $CuFe_2O_4-5\%$ CeO_2, and $CuFe_2O_4-20\%$ CeO_2 nanocomposites, respectively. The XRD results reveal a tetragonal structure for $CuFe_2O_4$ nanoparticles and for the corresponding $CuFe_2O_4-CeO_2$ nanocomposites. The addition of CeO_2 is characterized by the emergence of a (111) peak at 28.5° and a (220) peak at 47.4° (refer to Figure 8) belonging to pure ceria, and their intensities are found to increase with the increase in concentration of CeO_2. It is interesting to note that the 5% CeO_2 containing composites exhibit a prominent (311) peak (at 36.1°) of $CuFe_2O_4$ compared to 20% CeO_2 composites, which could be attributed to the incorporation of cerium ions in the spinel structure. The variation in the lattice parameter values of $CeO_2-CuFe_2O_4$ nanocomposites in comparison to $CuFe_2O_4$ nanoparticles also indicates the incorporation of cerium ions in the spinel lattice. In addition, the XRD pattern of these nanocomposites also reveals the presence of Bragg peaks corresponding to a pure CeO_2 phase, which could be attributed to the excess of CeO_2, which is not incorporated in the spinel structure. Due to the low CeO_2 content in the samples, unequivocal quantification of the different phases could not be performed.

The TEM and HRTEM images of the as-prepared $CuFe_2O_4$ nanoparticles and $CuFe_2O_4-5\%$ CeO_2 nanocomposites are shown in Figure 9. The TEM investigations show that the

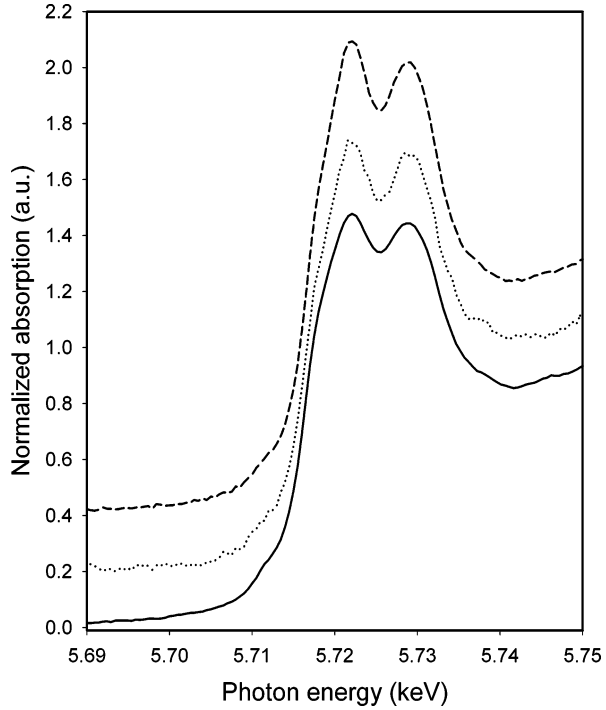

Figure 10. XANES region of $CuFe_2O_4-5\%$ CeO_2 (···) and $CuFe_2O_4-20\%$ CeO_2 (--) along with the reference CeO_2 (—) measured at the Ce L_{III}-edge.

$CuFe_2O_4$ samples exhibit the presence of 10−20 nm sized particles. The HRTEM images of $CuFe_2O_4$ confirmed the well-defined lattice fringes with a definite *d* value of 2.51 Å, which corresponds to the prominent plane of (311) for copper ferrite. The TEM and HRTEM images of the as-prepared $CuFe_2O_4-5\%$ CeO_2 composites indicate the particle size to be 5 nm. It also confirms the composite behavior of spinel (220) (observed at 31° in the XRD pattern presented in Figure 8a) with a *d* value of 2.92 Å and CeO_2 (111) with a *d* value of 3.33 Å, indicating the presence of two separate phases.

The XANES region of $CuFe_2O_4-CeO_2$ nanocomposites at the Cu and Fe K-edge are similar to those in $CuFe_2O_4$ nanoparticles. The edge energy and oxidation states determined from the XANES analysis at the Cu and Fe K-edges are summarized in Table 2. The analysis indicates that copper is in the +2 and iron is in the +3 oxidation state in the nanocomposites. Even though it was not possible to perform EXAFS analysis of the samples at the Ce L_{III}-edge, it was feasible to obtain a decent XANES region. From the XANES analysis it is possible to obtain information on the coordination geometry around the Ce atom, and any changes in the geometric structure of CeO_2 induced by $CuFe_2O_4$ would be reflected in changes in the XANES region. The XANES region of $CuFe_2O_4-CeO_2$ nanocomposites measured at the Ce L_{III}-edge is shown along with the reference CeO_2 in Figure 10. For clarity reasons, the spectra are shifted along the ordinate.

The XANES region of the 5 and 20% $CuFe_2O_4-CeO_2$ nanocomposites are similar to each other and resemble that of crystalline CeO_2. All the spectra show two clearly distinct absorption peaks, which are characteristic of CeO_2. These peaks are due to the resonance in the $2p \rightarrow 5d$ cross-section modified by the local density of the unoccupied states, resulting in the $5,\epsilon d$ final state.[63] The peaks arise from many-body final-state effects due to the mixing of multielectron configurations.[64] In addition, the similarity in the values for the absorption edge of the $CuFe_2O_4-CeO_2$ nanocomposites and CeO_2 reveals that cerium is in the +4 oxidation state in the nanocomposites.

4. Conclusion

The EXAFS and XANES investigations on $CuFe_2O_4$ nanoparticles reveal that the nanoparticles have a structure analogous to that of the bulk material. The studies indicate that all the copper ions occupy the octahedral sites, and the iron ions are distributed between the tetrahedral and octahedral sites. The XAFS investigations on $CuFe_2O_4-SnO_2$ and $CuFe_2O_4-CeO_2$ nanocomposites show that the incorporation of the tetravalent metal ions in the spinel structure does not alter the local environement around copper and iron ions in $CuFe_2O_4$ nanoparticles. In addition, the XRD pattern indicates $CuFe_2O_4$ as a single phase in the nanoparticles and shows the incorporation of tin and cerium ions in the spinel lattice besides the existence of MO_2 and $CuFe_2O_4$ phases in $CuFe_2O_4-MO_2$ nanocomposites. Furthermore, the TEM studies show that the as-synthesized particles are in nanometric sizes. The HRTEM investigations also confirm that $CuFe_2O_4$ exists as a single phase and reveal the composite nature of $CuFe_2O_4-MO_2$ materials.

Acknowledgment. HASYLAB at DESY, Hamburg, is gratefully acknowledged for the kind support for the synchrotron radiation experiments at beamline A1, and Dr. E. Welter is thanked for his support during the experiments. The authors express their gratitude to Prof. Dr. A. K. Shukla, Director, CECRI, Karaikudi, India for his keen interest in this work.

References and Notes

(1) O'Handley, R. C. *Modern Magnetic Materials—Principles and Applications*; Wiley: New York, 2000.
(2) Haefeli, U.; Schuett, W.; Teller, J.; Zborowski, M. *Scientific and Clinical Applications of Magnetic Carriers*; Plenum: New York, 1997.
(3) Morber, J. R.; Ding, Y.; Haluska, M. S.; Li, Y.; Liu, J. P.; Wang, Z. L.; Snyder, R. L. *J. Phys. Chem. B* **2006**, *110*, 21672.
(4) Sepelak, V.; Bergmann, I.; Feldhoff, A.; Heitjans, P.; Krumeich, F.; Menzel, D.; Litterst, F. J.; Campbell, S. J.; Becker, K. D. *J. Phys. Chem. C* **2007**, *111*, 5026.
(5) Song, Q.; Zhang, Z. J. *J. Phys. Chem. B* **2006**, *110*, 11205.
(6) Sivakumar, M.; Takami, T.; Ikuta, H.; Towata, A.; Yasui, K.; Tuziuti, T.; Kozuka, T.; Bhattacharya, D.; Iida, Y. *J. Phys. Chem. B* **2006**, *110*, 15234.
(7) Liu, C.; Zou, B.; Rondinone, A. J.; Zhang, Z. J. *J. Phys. Chem. B* **2000**, *104*, 1141.
(8) Wang, L.; Luo, J.; Fan, Q.; Suzuki, M.; Suzuki, I. S.; Engelhard, M. H.; Lin, Y.; Kim, N.; Wang, J. Q.; Zhong, C. J. *J. Phys. Chem. B* **2005**, *109*, 21593.
(9) Selvan, R. K.; Augustin, C. O.; Sanjeeviraja, C.; Pol, V. G.; Gedanken, A. *Mater. Chem. Phys.* **2006**, *99*, 109.
(10) Dey, A.; De, A.; De, S. K. *J. Phys.: Condens. Matter* **2005**, *17*, 5895.
(11) Shi, W.; Zeng, H.; Sahoo, Y.; Ohulchanskyy, T. Y.; Ding, Y.; Wang, Z. L.; Swihart, M.; Prasad, P. N. *Nano Lett.* **2006**, *6*, 875.
(12) Nilsen, M. H.; Nordhei, C.; Ramstad, A. L.; Nicholson, D. G.; Poliakoff, M.; Cabanas, A. *J. Phys. Chem. C* **2007**, *111*, 6252.
(13) Carta, D.; Mountjoy, G.; Navarra, G.; Casula, M. F.; Loche, D.; Marras, S.; Corrias, A. *J. Phys. Chem. C* **2007**, *111*, 6308.
(14) Henderson, C. M. B .; Charnock, J. M .; Plant, D. A . *J. Phys.: Condens. Matter* **2007**, *19*, 076214.
(15) Gomes, J. A.; Sousa, M. H.; da Silva, G. J.; Tourinho, F. A.; Mestnik-Filho, J.; Itri, R.; Depeyrot, J. *J. Magn. Magn. Mater.* **2006**, *300*, e213.
(16) Huang, Z.; Zhu, Y.; Zhang, J.; Yin, G. *J. Phys. Chem. C* **2007**, *111*, 6821.
(17) Qi, J. Q.; Chen, W. P.; Leu, M.; Wang, Y.; Tian, H. Y.; Li, L. T.; Chan, H. L. W. *Nanotechnology* **2005**, *16*, 3097.
(18) Du, J.; Liu, Z.; Wu, W.; Li, Z.; Han, B.; Huang, Y. *Mater. Res. Bull.* **2005**, *40*, 928.
(19) (a) Banerjee, M.; Roy, A. *J. Nanosci. Nanotechnol.* **2007**, *7*, 1997. (b) Gajbhiye, N. S.; Balaji, G.; Bhattacharyya, S.; Ghafari, M. *Hyperfine Interact.* **2004**, *156−157*, 57.
(20) Goya, G. F. *J. Mater. Sci. Lett.* **1997**, *16*, 563.
(21) Rajic, N.; Ceh, M.; Gabrovsek, R.; Kaucic, V. *J. Am. Ceram. Soc.* **2002**, *85*, 17191.
(22) Roy, S.; Ghose, J. *J. Magn. Magn. Mater.* **2006**, *307*, 32.

(23) Tao, S.; Gao, F.; Liu, X.; Sorensen, O. T. *Mat. Sci. Eng. B* **2000**, *77*, 172.
(24) Shin, H. S.; Choi, S. C.; Jung, K. D.; Han, S. H. *Chem. Mater.* **2001**, *13*, 1238.
(25) NuLi, Y. N.; Qin, Q. Z. *J. Power Sources* **2005**, *142*, 292.
(26) Faungnawakij, K.; Tanaka, Y.; Shimoida, N.; Fukunaga, T.; Kikuchi, R.; Eguchi, K. *Appl. Catal., B* **2007**, *74*, 144.
(27) Zhang, G.; Qu, J. ; Liu, H.; Cooper, A. T.; Wu, R. *Chemosphere* **2007**, *68*, 1058.
(28) Goya, G. F.; Rechenberg, H. R.; Jiang, J. Z. *J. Appl. Phys.* **1998**, *84*, 1101.
(29) Goodenough, J. B.; Loeb, A. L. *Phys. Rev.* **1955**, *98*, 391.
(30) Bertaut, E. F. *J. Phys. Radium* **1951**, *12*, 252.
(31) McClure, D. S. *J. Phys. Chem. Solids* **1957**, *3*, 318.
(32) Dunitz, J. D.; Orgel, L. E. *J. Phys. Chem. Solids* **1957**, *3*, 20.
(33) Jayadevan, B.; Tohji, K.; Nakatsuka, K.; Narayanasamy, A. *J. Magn. Magn. Mater.* **2000**, *217*, 99.
(34) Selvan, R. K.; Augustin, C. O.; Sanjeeviraja, C.; Prabhakaran, D. *Solid State Commun.* **2006**, *137*, 512.
(35) Selvan, R. K.; Kalaiselvi, N.; Augustin, C. O.; Doh, C. H.; Sanjeeviraja, C. *J. Power Sources* **2006**, *157*, 522.
(36) Teo, B. K. *EXAFS: Basic Principles and Data Analysis*; Springer: Berlin, 1986.
(37) Koningsberger, D. C.; Prins, R. *X-ray Absorption: Principles, Applications, Techniques of EXAFS, SEXAFS and XANES*; Wiley: New York, 1988.
(38) Stöhr, J. *NEXAFS Spectroscopy*; Springer: Berlin, 1996.
(39) Biaconi, A. In *EXAFS and Near Edge Structure II*; Hodgson, K. O., Hedman, B., Penner-Hahn, J. E., Eds.; Springer Proceedings in Physics; Springer: Berlin, 1984.
(40) Wong, F.; Lytle, F. W.; Messmer, R. P.; Maylotte, D. H. *Phys. Rev. B* **1984**, *30*, 5596.
(41) Selvan, R. K.; Augustin, C. O.; Berchmans, L. J.; Saraswathi, R. *Mater. Res. Bull.* **2003**, *38*, 41.
(42) Ressler, T. *J. Phys. IV* **1997**, *C2*−*C7*, 269.
(43) Newville, M.; Livins, P.; Yakoby, Y.; Rehr, J. J.; Stern, E. A. *Phys. Rev. B* **1993**, 14126.
(44) Gurman, S. J.; Binstead, N.; Ross, I. *J. Phys. C* **1986**, *19*, 1845.
(45) Corrias, A.; Mountjoy, G.; Piccaluga,G.; Solinas, S. *J. Phys. Chem. B* **1999**, *103*, 10081.
(46) Asahi, R.; Taga, Y.; Mannstadt, W.; Freeman, A. J. *Phys. Rev. B* **2000**, *61*, 7459.
(47) Chen, L. X.; Liu, T.; Thurnauer, M. C; Csencsits, R.; Rajh, T. *J. Phys. Chem. B* **2002**, *106*, 8539.
(48) Grunes, L. A. *Phys. Rev. B* **1983**, *27*, 2111.
(49) Ankudinov, A. L.; Rehr, J. J.; Bare, S. R. *Chem. Phys. Lett.* **2000**, *316*, 495.
(50) Biaconi, A.; Davoli, I.; Della Longa, S.; Garcia, J.; Garg, K. B.; Kotani, A.; Marcelli, A. In *Theoretical and Experimental Aspects of Valence Fluctuations and Heavy Fermions*; Gupta, L. C., Malik, S. K., Eds.; Plenum: New York, 1987.
(51) Harris, V. G.; Koon, N. C.; Williams, C. M.; Zhang, Q.; Abe, M.; Kirkland, J. P.; McKeown, D. A. *IEEE Trans. Magn.* **1995**, *31*, 3473.
(52) Prince, E.; Treuting, R. G. *Acta Crystallogr.* **1956**, *9*, 1025.
(53) Harris, V. G.; Koon, N. C.; Williams, C. M.; Zhang, Q.; Abe, M.; Kirkland, J. P. *Appl. Phys. Lett.* **1996**, *68*, 2082.
(54) Bhongale, G. M.; Sapre, V. B.; Kulkarni, D. K. *Bull. Mater. Sci.* **1993**, *16*, 243.
(55) Sahastabudhe, V.; Vaingankar, A. S. *Solid State Commun.* **1982**, *43*, 299.
(56) Yang, A.; Chen, Z. ; Zuo, X.; Arena, D. ; Kirkland, J. ; Vittoria, C.; Harris, V. G. *Appl. Phys. Lett.* **2005**, *86*, 252510.
(57) Ohnishi, H.; Teranishi, T. *J. Phys. Soc. Jpn.* **1961**, *16*, 35.
(58) Nanba, N. *J. Appl. Phys.* **1978**, *49*, 2950.
(59) Tranquada, J. M.; Heald, S. M.; Moodenbaugh, A. R. *Phys. Rev. B* **1987**, *36*, 5263.
(60) Shimizu, K.; Maeshima, H.; Yoshida, H.; Satsuma, A.; Hattori, T. *Phys. Chem. Chem. Phys.* **2001**, *3*, 862.
(61) Waychunas, G. A.; Apted, M. J.; Brown, G. E., Jr. *Phys. Chem. Miner.* **1983**, *10*, 1.
(62) (a) Scherrer, P. *Nachr. Ges. Wiss. Goettingen* **1918**, 96. (b) Klug H. P.; Alexander, L. E. *X-Ray Diffraction Procedures for Polycrystalline and Amorphous Materials*; Wiley: New York, 1974.
(63) Soldatov, A.; Ivanchenko, T. S.; Longa, S. D.; Kotani, A.; Iwamoto, Y.; Bianconi, A. *Phys. Rev. B* **1994**, *50*, 5074.
(64) Bianconi, A.; Marcelli,A.; Dexpert, H.; Karnatak, R.; Kotani, A.; Jo, T.; Petiau, J. *Phys. Rev. B* **1987**, *35*, 806.